Monthly Notices of the ROYAL ASTRONOMICAL SOCIETY

MNRAS **513,** 1858–1866 (2022)
Advance Access publication 2022 April 13

https://doi.org/10.1093/mnras/stac1031

The northern cross fast radio burst project – II. Monitoring of repeating FRB 20180916B, 20181030A, 20200120E, and 20201124A

M. Trudu [1,2]★ M. Pilia,[2] G. Bernardi,[3,4,5] A. Addis,[6] G. Bianchi,[3] A. Magro [7] G. Naldi,[3] D. Pelliciari,[3,8] G. Pupillo,[3] G. Setti,[3,8] C. Bortolotti,[3] C. Casentini,[9,10] D. Dallacasa,[3,8] V. Gajjar,[11] N. Locatelli,[12] R. Lulli,[3] G. Maccaferri,[3] A. Mattana,[3] D. Michilli [13,14] F. Perini,[3] A. Possenti,[1,2] M. Roma,[3] M. Schiaffino,[3] M. Tavani[9,15] and F. Verrecchia[16,17]

[1]*Universitá degli Studi di Cagliari, Dipartimento di Fisica, SP Monserrato-Sestu km 0.7, I-09042 Monserrato (CA), Italy*
[2]*INAF-Osservatorio Astronomico di Cagliari, via della Scienza 5, I-09047, Selargius (CA), Italy*
[3]*INAF-Istituto di Radio Astronomia, via Gobetti 101, I-40129 Bologna, Italy*
[4]*South African Radio Astronomy Observatory, Black River Park, 2 Fir Street, Observatory, Cape Town, 7925, South Africa*
[5]*Department of Physics and Electronics, Rhodes University, PO Box 94, Makhanda, 6140, South Africa*
[6]*INAF-Osservatorio di Astrofisica e Scienza dello Spazio di Bologna, Via Piero Gobetti, 93/3, I-40129, Bologna, Italy*
[7]*Institute of Space Sciences and Astronomy (ISSA), University of Malta, Msida MSD 2080, Malta*
[8]*Dipartimento di Fisica e Astronomia, Universitá di Bologna, Via Gobetti 93/2, I-40129 Bologna, Italy*
[9]*INAF/IAPS, via del Fosso del Cavaliere 100, I-00133 Roma (RM), Italy*
[10]*INFN Sezione di Roma 2, via della Ricerca Scientifica 1, I-00133 Roma (RM), Italy*
[11]*Department of Astronomy, University of California Berkeley, Berkeley, CA 94720, USA*
[12]*Max-Planck-Institut für Extraterrestrische Physik (MPE), Giessenbachstrasse 1, D-85748 Garching bei München, Germany*
[13]*MIT Kavli Institute for Astrophysics and Space Research, Massachusetts Institute of Technology, 77 Massachusetts Ave, Cambridge, MA 02139, USA*
[14]*Department of Physics, Massachusetts Institute of Technology, 77 Massachusetts Ave, Cambridge, MA 02139, USA*
[15]*Universitá degli Studi di Roma 'Tor Vergata', via della Ricerca Scientifica 1, I-00133 Roma (RM), Italy*
[16]*SSDC/ASI, via del Politecnico snc, I-00133 Roma (RM), Italy*
[17]*INAF-Osservatorio Astronomico di Roma, via Frascati 33, I-00078 Monte Porzio Catone (RM), Italy*

Accepted 2022 April 7. Received 2022 March 8; in original form 2022 February 1

ABSTRACT

In this work, we report the results of a 19-month fast radio burst observational campaign carried out with the north–south arm of the Medicina Northern Cross radio telescope at 408 MHz in which we monitored four repeating sources: FRB20180916B, FRB20181030A, FRB20200120E, and FRB20201124A. We present the current state of the instrument and the detection and characterization of three bursts from FRB20180916B. Given our observing time, our detections are consistent with the event number we expect from the known burst rate (2.7 ± 1.9 above our 10σ, 38 Jy ms detection threshold) in the 5.2 d active window of the source, further confirming the source periodicity. We detect no bursts from the other sources. We turn this result into a 95 per cent confidence level lower limit on the slope of the differential fluence distribution α to be $\alpha > 2.1$ and $\alpha > 2.2$ for FRB20181030A and FRB20200120E, respectively. Given the known rate for FRB20201124A, we expect 1.0 ± 1.1 bursts from our campaign, consistent with our non-detection.

Key words: methods: observational – radio continuum: transients – fast radio bursts.

1 INTRODUCTION

Fast radio bursts (FRBs) are millisecond-duration radio transients with high fluences ($\sim$1–100 Jy ms) and (mostly) extragalactic origin (Cordes & Chatterjee 2019; Petroff, Hessels & Lorimer 2019, 2022). The discovery of repeating FRBs (or repeaters, Spitler et al. 2016; CHIME/FRB Collaboration et al. 2019c,a) has opened the window to in-depth studies of some of these sources, which have provided the most stringent constraints to FRB models so far. Not all repeaters seems to behave similarly and possess the same kind of progenitor.

The first known repeater, FRB20121102A[1] (Spitler et al. 2014, 2016) appears to be a very active and, possibly, very young source, located in the star-forming region of a dwarf galaxy at $z = 0.193$ (Chatterjee et al. 2017; Marcote et al. 2017; Tendulkar et al. 2017), corresponding to a luminosity distance of $\sim$1 Gpc. The presence of a persistent radio source co-located with the FRB emission (Marcote et al. 2017), the observation of significant variations in dispersion measure (DM) and rotation measure (Michilli et al. 2018), and the high number of detections at high frequencies (up to 8 GHz, Gajjar et al. 2018; CHIME/FRB Collaboration et al. 2019b) compared to

★ E-mail: trudumatteo@outlook.com

[1]FRB sources are named according to the Transient Name Server (https://www.wis-tns.org/).

© 2022 The Author(s)
Published by Oxford University Press on behalf of Royal Astronomical Society

Downloaded from https://academic.oup.com/mnras/article/513/2/1858/6567872 by CNR user on 26 May 2022

a low number (only one) of detections at low frequencies (below 1 GHz, Josephy et al. 2019), all concurred to interpret this source as a very young compact object surrounded by a dense medium. In particular, many of the models relied on an active magnetar, as the progenitor of FRB20121102A, possibly residing in its wind nebula (see Zhang 2020).

The third discovered repeater, FRB20180916B (CHIME/FRB Collaboration et al. 2019a), was also soon found to be a very active source, which was localized to the outskirts of a star forming region in a nearby massive spiral galaxy ($z = 0.0337$, Marcote et al. 2020; Tendulkar et al. 2021). A high activity rate is the main common feature between the two sources. FRB20180916B is not coincident with a persistent source, with an upper limit on the luminosity that is 40 times lower than the persistent source associated with FRB20121102A; no significant DM or RM variations have been observed in time and its emission seems prominent at low frequencies (below 1 GHz, see e.g. Chawla et al. 2020; Marcote et al. 2020; Pastor-Marazuela et al. 2021; Pilia et al. 2020; Pleunis et al. 2021), while it has never been observed above 2 GHz (Pearlman et al. 2020). FRB20180916B was also the first repeater for which a periodicity was established (CHIME/FRB Collaboration et al. 2020), which afterwards led to a similar finding for FRB20121102A (Rajwade et al. 2020). FRB20180916B has a period of 16.33 days (refined by Pleunis et al. 2021) with an active window of ± 2.6 d around its peak phase. FRB20121102A, on the other hand, has a period of 161 d (refined by Cruces et al. 2021) with a 54 per cent duty cycle. The discovery of periodicity, in particular in the case of the nearby and frequently active FRB20180916B has made extensive sensitive follow-up possible and rewarding, allowing for an unprecedented availability of radio data on this source.

The study of FRBs has received significant momentum from the advent of the CHIME telescope (CHIME/FRB Collaboration et al. 2018), operating as a transit instrument and being able to monitor the transient sky virtually full time and with real-time capability to analyse the data and trigger alerts. The success of the CHIME/FRB experiment, which led in one year to the discovery of ∼500 FRBs, about 20 of which being repeating sources (The CHIME/FRB Collaboration et al. 2021), demonstrated that field of view and time on sky are two strong requirements to carry out extensive FRB searches. The experience that has built up on that, and on the continuous study of repeaters in particular, has further highlighted the need of an immediate reaction on possible burst alerts in order to both understand multifrequency or chromatic properties of the radio emission and try to catch the elusive multiwavelength counterpart of this emission.

The Northern Cross (NC) radio telescope, located in Medicina near Bologna (Italy), is a transit telescope which operates at 408 MHz (*P* band) with an observational bandwidth of 16 MHz. It is a *T*-shaped interferometer with two arms aligned along the north–south and east–west directions. The north–south arm has been going through a software and hardware upgrade which made it suitable for FRB observations, whereas the east–west arm is not currently in use. The system and its survey capabilities are described in Locatelli et al. (2020, hereafter Paper I).

In this paper, we present the results of an observational campaign, spread over about 19 months, which monitored four repeaters, mainly performed during known or presumed active phases in the NC observing band. The selected targets are FRB20180916B, FRB20181030A, FRB20200120E, and FRB20201124A. The paper is organized as follows. In Section 2, we report the current state of system deployed at the NC for the FRB data acquisition and the FRB detection pipeline; in Section 3, we describe the targets selected in this observational campaign; in Section 4, we report the results obtained from this monitoring, and in Section 5, we provide a short summary.

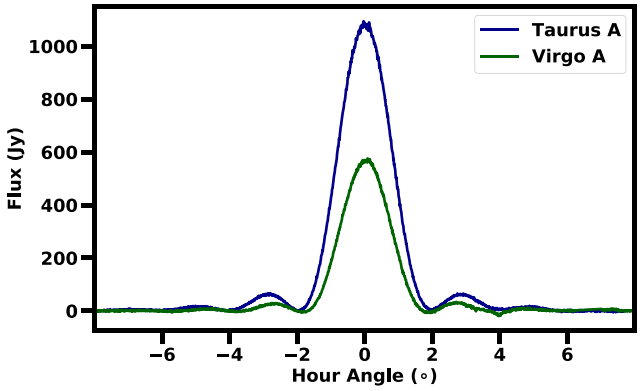


Figure 1. Calibrated drift scans of the astronomical sources, Taurus A and Virgo A, used for the SEFD estimation, observed with the eight-cylinders array beam, referred to the channel corresponding at the central frequency of 408.45 MHz. The profile clearly shows the main and the first lobe of the array beam.

2 SYSTEM DESCRIPTION

2.1 Data Acquisition System

In this section we provide a brief overview of the NC system as presented in Paper I and describe the most recent updates. The north–south arm of the NC used in our observations includes 64 parabolic cylinders. Each cylinder illuminates four groups of 16 dipoles each, for a total of 64 dipoles. Signals from each of the 16 dipoles are combined together analogically and fed to a single receiver. Until 2021 March 21, six cylinders were used, for a total of twenty four receivers, whereas afterwards 8 cylinders were equipped and used for a total of 32 receivers. Signals from the receivers were digitized, channelized, combined into a single beam and then written to disc. Unlike the system used in Paper I, we have routinely implemented a second channelization stage with a windowed FFT that effectively leads to a power stream with a 138.24 μs time resolution and a 14.468 kHz frequency resolution in order to reduce the intra-channel smearing for high DM events. The oversampling polyphase filterbank architecture of the first stage channelizer used in Paper I (see Comoretto et al. 2017 for details) causes an overlap between adjacent coarse channels by a factor of 5/32 (oversampling of 32/27). The overlapping portions of each pair of adjacent channels, that coincide with the filter transition region in the channel edges, are discarded and the resulting bandpass, consisting of 1024 fine spectral channels, is seamless and flat. The 32 bit time series of each frequency channel are then equalized and rescaled, over discrete time intervals of 10 s, in order to correctly represent 6σ samples with 16 bit data, using `digifil` from the DSPSR toolkit (van Straten & Bailes 2011). Output data are saved to disc using the SIGPROC Filterbank file format (Lorimer 2011).

During the observing campaign, we used the eight-cylinder system to observe the transit of two bright sources, Taurus A and Virgo A, for 2 h each in order to further characterize the System Equivalent Flux Density (SEFD), following up on the estimates derived in Paper I from observations of the PSR B0329 + 54 pulsar. Fig. 1 shows the corresponding transit observations, where the telescope was steered towards the corresponding declination of each source. We perform

Downloaded from https://academic.oup.com/mnras/article/513/2/1858/6567872 by CNR user on 26 May 2022

Table 1. Astronomical sources used as calibrators. SEFDs are estimated for groups of 16 dipoles (i.e. one receiver). The SEFD for six and eight cylinders can be obtained by multiplying for the corresponding number of receivers 24 and 32, respectively.

Source	Sky position (RA J2000, Dec. J2000)	Starting time UT	SEFD (Jy)
Taurus A	$05^{h}34^{m}31\overset{s}{.}940$, $+22^{\circ}00'52\overset{''}{.}20$	2021/04/13 14:21:03	9000 ± 400
Virgo A	$12^{h}30^{m}49\overset{s}{.}423$, $+12^{\circ}23'28\overset{''}{.}05$	2021/04/01 22:03:02	7800 ± 180

a standard on-off observation, where we estimate the background contribution as the average of the power away from source, i.e. for hour angles $>|6^{\circ}|$, and subtract it from the observed power when the source is within the main beam. We then fit a Gaussian model to the profile full width at half-maximum (FWHM) for 21 frequency channels equally spaced across the 16 MHz bandwidth. Taurus A and Virgo A are assumed to be 1080 and 569 Jy at 408 MHz, respectively (Perley & Butler 2017), and the best fit to the curve peak provides the conversion from counts to Jy for each channel. The SEFD is derived from the rms of the calibrate power away from sources, i.e. for hour angle $>|6^{\circ}|$. The SEFD is found to vary up to 20 per cent across the bandwidth, a negligible variation for the purpose of the current analysis. We eventually average the SEFD estimates to obtain a band-averaged value (Table 1).

We note a slight dependence of the SEFD with the Galactic latitude, varying by $\sim$ 14 per cent from the Galactic plane (Taurus A is at a $\sim -5^{\circ}$ Galactic latitude) to high Galactic latitudes (Virgo A is at a $\sim +74^{\circ}$ Galactic latitude). This dependence is qualitatively expected as the sky temperature contribution to the SEFD increases towards the plane. At the same time, our results indicate that the sky temperature contribution to the SEFD is minor. For the purpose of this work, we will adopt the same SEFD* estimate for all FRB source, obtained by averaging the Taurus A and Virgo A values:

$$\mathrm{SEFD}^{*} = 8400 \pm 420 \ \mathrm{Jy}. \quad (1)$$

2.2 Single pulse search pipeline

The search for FRB candidates is currently performed through an adaptation of the SPANDAK pipeline (Gajjar et al. 2018). The pipeline uses RFIFIND from PRESTO (Ransom, Eikenberry & Middleditch 2002) to prepare the radio frequency interference (RFI) mask, which is then used by HEIMDALL (Barsdell et al. 2012) in order to flag out the noisiest frequency channels. The data are then searched by SPANDAK through HEIMDALL across a DM range from 0 to 1000 pc cm^{-3} with a signal-to-noise ratio (S/N) loss tolerance in each DM trial of 10 per cent and the dedispersed time series have been convolved with a maximum boxcar of 1024 samples.

Candidates found by SPANDAK are then further selected according to the S/N, the DM, the width of the burst Δt, the maximum number N_w of allowed candidates found within a time window w centred at the time of the candidate and the minimum number N_m of distinct boxcar/DM trials (members) clustered into a candidate. Candidates which agree with the following criteria are classified as plausible FRB candidates:

$$\begin{aligned} \mathrm{S/N} &\geq 10; \\ \mathrm{DM} &\geq 10 \ \mathrm{pc\ cm^{-3}}; \\ \Delta t &\leq 141.6 \ \mathrm{ms}; \\ N_{w=4\ \mathrm{s}} &\leq 2; \\ N_m &\geq 10. \end{aligned} \quad (2)$$

Filtered candidates are then validated by the artificial neural network classifier FETCH (Agarwal et al. 2020) and, eventually, manually inspected.

3 SELECTED TARGETS

We report the results of the observational campaign conducted between 2020 January 16 and 2021 August 29 for the following four repeating FRB sources: FRB20180916B, FRB20181030A, FRB20200120E, and FRB20201124A. Sources were selected for their proximity (as initially suggested by their low DM values and later confirmed by their localization) and therefore as favourable targets both for our new system and for the multiwavelength campaign that included the NC (see e.g. Pilia et al. 2020; Tavani et al. 2020, 2021).

The whole NC campaign is summarized in Fig. 2, including all the observations performed for the monitored sources at the various epochs. We highlight the time when the transition between the six-cylinder system and the eight-cylinder system occurred. In the following sections, we will describe the targets in more detail.

3.1 FRB20180916B

FRB20180916B is our main target and was observed for a total of $\sim$180 h throughout the campaign. Starting in January 2020, when its periodic activity was announced (CHIME/FRB Collaboration et al. 2020), the NC observed FRB20180916B regularly during its active cycles. FRB20180916B has a periodic activity of $\sim$16 d with an active window of 5.2 d and we observed the source for about seven days each cycle, beginning one day before the period (predicted in the CHIME/FRB bandwidth) in order to match the multiwavelength campaign from the Swift and AGILE satellites, trying to catch earlier emission (Casentini et al. 2020; Tavani et al. 2021; Verrecchia et al. 2021). The primary aim of these observations was indeed to find theoretically predicted multiwavelength counterparts (Lyubarsky 2014; Beloborodov 2017; Kumar, Lu & Bhattacharya 2017; Ghisellini & Locatelli 2018; Metzger, Margalit & Sironi 2019; Lu, Kumar & Zhang 2020; Lyutikov & Popov 2020), looking for time coincidences with other instruments (see Nicastro et al. 2021 for an updated review).

3.2 FRB20181030A

FRB20181030A is the fourth known repeater, with two bursts detected by CHIME/FRB in 2018 October (CHIME/FRB Collaboration et al. 2019a) and seven new bursts detected in 2020 January. It has a DM $\sim$103 pc cm^{-3} and a maximum estimated redshift of $z = 0.05$. The star-forming spiral galaxy NGC 3252 ($z \sim 0.004$) has been identified as its most auspicious host among seven plausible galaxies within the 90 per cent confidence localization region (Bhardwaj et al. 2021b).

Downloaded from https://academic.oup.com/mnras/article/513/2/1858/6567872 by CNR user on 26 May 2022

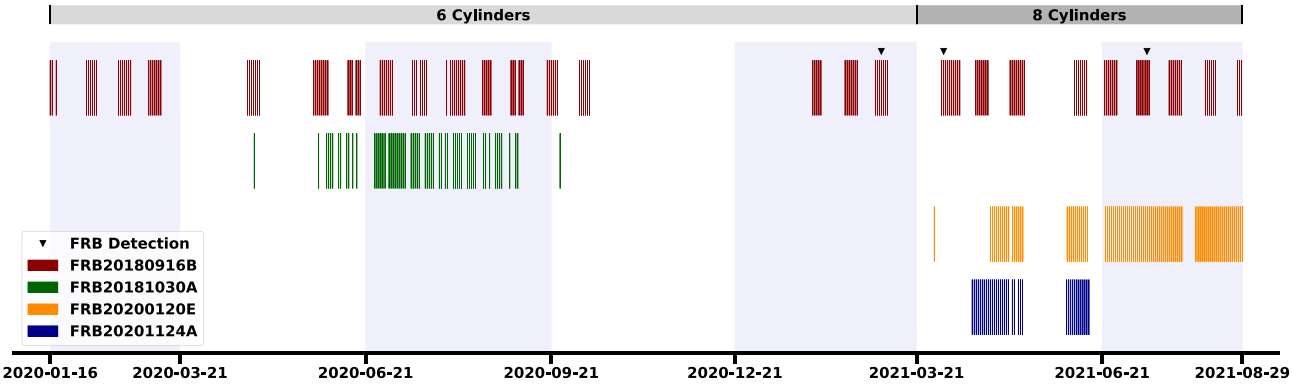


Figure 2. Observational campaign of the NC telescope. Coloured bars represent observations performed for each FRB source as a function of the day of the year. Black triangles indicate days when FRB were detected. Seasons of the year have been depicted as alternated white and lavender rectangles, to help the eye. The top grey and dark grey bars represent, respectively, the time in which the six-cylinders and eight-cylinders system were used during the campaign.

Due to its small DM value, with an associated distance of ∼20 Mpc, FRB20181030A has been monitored, on an approximately daily basis, from 2020 April until 2020 September, for a total of 93 h, as an interesting target for multiwavelength observations despite the initial lack of localization. This source, however, has shown very little activity over the last years, compared to FRB20180916B: only nine bursts were detected by CHIME since its discovery, with a fluence smaller than 10 Jy ms.

3.3 FRB20200120E

FRB20200120E is a repeater with DM ∼ 88 pc cm^{-3}(Bhardwaj et al. 2021a), initially localized in the outskirts of M81, a spiral galaxy with a distance of ∼ 3.6 Mpc (Freedman et al. 1994) and afterwards precisely localized in a globular cluster within M81 with the detection of five bursts from the source at 1.4 GHz (*L* band) by the European VLBI Network (EVN) (Kirsten et al. 2021). Thanks to the relative proximity of the source and also thanks to its high Galactic latitude (∼41.2°), which makes the scattering broadening due to the Milky Way interstellar medium negligible, an ultra-high-time resolution analysis of the five bursts detected by Kirsten et al. (2021) has been performed, showing that this source can produce nanosecond duration isolated bursts with 10^{41} K brightness temperature (Nimmo et al. 2021a, Majid et al. 2021), similar to the Crab pulses (Hankins et al. 2003). This unprecedented finding marked a bridge between young Galactic pulsars and magnetars and the more distant FRBs in terms of burst durations and luminosities (see in particular fig. 3 from Nimmo et al. 2021a).

This target was included in the selection being the closest known repeater so far. Analogously to FRB20181030A, we monitored this source about once a day from 2021 March to the last day of the campaign reported in this paper, for a total observing time of ∼109 h.

3.4 FRB20201124A

FRB20201124A is a repeater with DM ∼410 pc cm^{-3}, discovered by CHIME/FRB in 2020 November. It had a very active phase between 2021 March and May (CHIME/FRB Collaboration 2021; Lanman et al. 2021), with a plethora of follow-up detections by other radio telescopes (Kumar et al. 2021; Law et al. 2021; Marcote et al. 2021; Xu et al. 2021; Wharton et al. 2021) at both *P* and *L* bands, with an initial localization of the source by ASKAP (Day et al. 2021), FAST (Xu et al. 2021), uGMRT (Wharton et al. 2021), and VLA (Law et al. 2021) and further refined, with a milliarcsecond precision, by the EVN (Nimmo et al. 2021b). It was localized in a nearby ($z \sim 0.098$) (Fong et al. 2021) galaxy with a high star formation rate which suggests a new-born magnetar as the most likely progenitor (Piro et al. 2021). We monitored this source daily from 2021 April to 2021 June for a total observing time of 68 h.

4 BURSTS DETECTED

We report the detection of three bursts from FRB20180916B: B1, B2, and B3, from now onwards. These bursts happened on 2021 March 3, 2021 April 3, and 2021 July 13, respectively. Table 2 contains the observed properties of the detected bursts. Fig. 3 shows the dedispersed waterfall plots of B1, B2, and B3, obtained with the fit-optimized DM reported in Table 2.

4.1 Burst characterization

The properties of the detected bursts, that is their time of arrival (TOA), the width Δt, the best DM and the scattering time τ have been computed by making a fit of the spectrotemporal data array. We use, as a template for the burst in the time domain, a Gaussian function convolved with an exponential decay function (McKinnon 2014) and a Gaussian function for the burst in the frequency domain. The fit procedure has been performed using the software package `BURSTFIT`, a detailed description of this package can be found in Aggarwal et al. (2021).

The flux density S of the incoming radiation from the source is then computed by using a modified version of the standard radiometer equation for single pulses (Lorimer & Kramer 2005):

$$S = \mathrm{S/N}\,\frac{\mathrm{SEFD}^*}{A\sqrt{N_p N_c (1-\xi)\Delta\nu_{\rm ch}\Delta t}}\,\zeta\,(\mathrm{TOA})\,. \qquad (3)$$

Here, S/N is the integrated signal-to-noise ratio of the frequency averaged time series, $A = 24$ or 32 is a geometric factor which takes into account the ratio between the collecting area of the six or eight cylinders system and one receiver (see Paper I for further details), $N_p = 1$ is the number of polarizations, $N_c = 1024$ is the number of spectral channels of the observation, ξ is the fraction of channels excised as RFI, and $\Delta\nu_{\rm ch}$ is the channel width. The multiplicative factor ζ(TOA) takes into account the primary beam attenuation at the burst TOA.

Downloaded from https://academic.oup.com/mnras/article/513/2/1858/6567872 by CNR user on 26 May 2022

Table 2. Properties of the detected bursts of FRB20180916B from the NC campaign. The second column reports the percentage of channels excised as RFI; the third, the fourth, and the fifth columns report the barycentric (∞ MHz) time of arrival of the bursts as MJD, UT, and phase of the activity period of FRB20180916B (see Section 4.2); the sixth column reports the fit-optimized DM; the seventh column the S/N; the eighth column reports the FWHM burst duration in ms; the ninth column reports the scattering time computed with respect to the reference frequency of 408 MHz; the tenth and eleventh columns report, respectively, the flux densities and the fluences of the bursts.

	ξ (per cent)	TOA (MJD)	TOA (UT)	ϕ	DM (pc cm^{-3})	S/N	Δt (ms)	τ (ms)	S (Jy)	F (Jy ms)
B1	2	59276.5954859605(4)	2021-03-03 14:17:29.987(1)	0.554 ± 0.008	$349.28^{+0.25}_{-0.26}$	14.5	$4.76^{+0.57}_{-0.63}$	/	20 ± 2	96 ± 14
B2	12	59307.5148011862(7)	2021-04-03 12:21:18.822(4)	0.447 ± 0.007	$349.57^{+0.36}_{-0.36}$	21.7	$5.95^{+0.75}_{-0.68}$	<3.6	22 ± 3	135 ± 19
B3	8	59408.2528584486(4)	2021-07-13 06:04:06.970(6)	0.616 ± 0.009	$349.64^{+0.35}_{-0.37}$	12.5	$4.37^{+0.45}_{-0.45}$	/	16 ± 1	71 ± 8

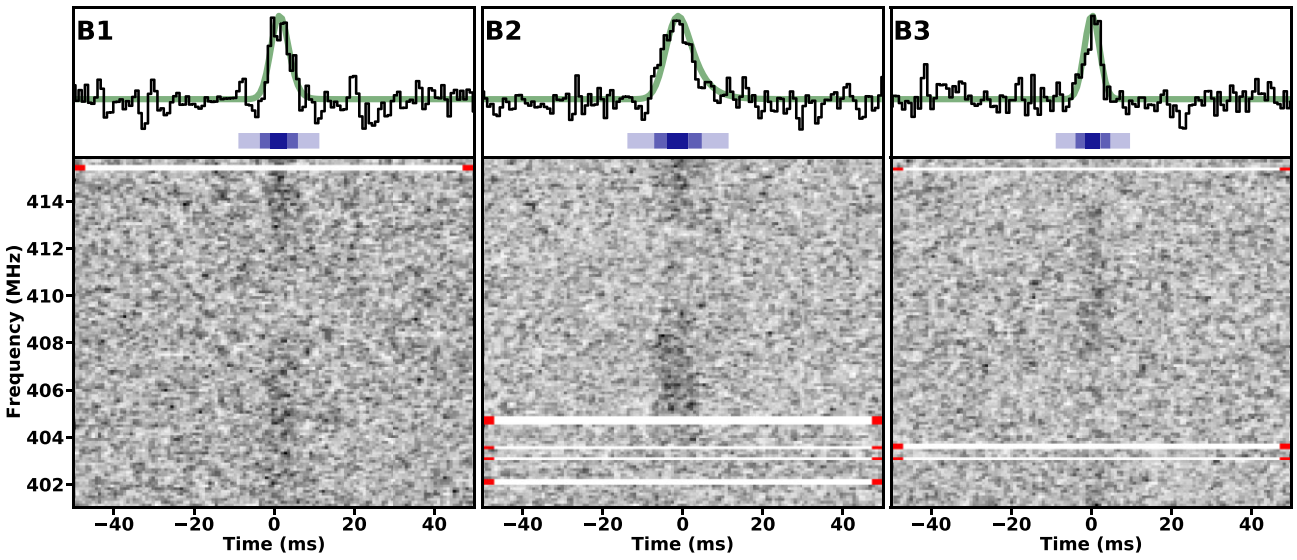


Figure 3. Bursts observed from FRB20180916B (B1, B2, and B3) during the NC observational campaign. Bottom (left, centre, and right) panels represent the dynamic spectrum of the signal, whereas the top (left, centre, and right) are the frequency averaged time-series (black curves) and the best-fitting model (green curves) of the three bursts. For each burst the 2σ, FWHM, and 10σ widths are displayed as blue rectangles. The bursts are, from left to right, ordered by time and each of them has been dedispersed according to the obtained best DM (see Table 2). For a better display, data are down-sampled to have 128 frequency channels with a 0.116 MHz width each and 128 time bins with size of 0.78 ms. Horizontal white rows (highlighted with red ticks) are flagged channels due to RFI.

The estimated fluences F of the bursts were calculated as the product between the flux density S and the duration of the burst Δt.

4.2 Bursts properties

The top panels of Fig. 3 show the frequency-averaged time series of B1, B2, and B3. We obtain a significant measurement for the scattering time only for B2, with a value of 3.6 ms at 408 MHz. This would correspond to ~ 0.8 ms at 600 MHz, consistent with previous scattering time measurements reported for this source (CHIME/FRB Collaboration et al. 2019a). However, we consider this value as an upper limit as Marcote et al. (2020) and Pastor-Marazuela et al. (2021) placed a tighter constraint on the scattering time-scale of the order of 3 μs at 1.7 GHz, similar to the NE2001 (Cordes & Lazio 2002) prediction of 2 μs. Our estimate would correspond to 10 μs at 1.7 GHz. Hence, we conclude that this apparent scattering tail, as showed in the model for B2 in Fig. 3, could be originated by the presence of not resolvable sub-bursts (CHIME/FRB Collaboration et al. 2019a).

None of the three detected burst show peculiar spectrotemporal features (bottom panels of Fig. 3), that is the typical downward drift of the signal in the time-frequency plane (oftentimes called 'sad trombone effect') as often reported for repeater sources (CHIME/FRB Collaboration et al. 2019b; Hessels et al. 2019; Pleunis et al. 2021), as can be seen from the dynamic spectra in Fig. 3.

Fig. 4 shows the span of our observations and the occurrence of B1, B2, and B3 as a function of the relative phase ϕ, during the activity cycles of FRB20180916B. The phases are obtained folding the data at the nominal period of 16.33 d taking a starting phase $\phi_0 = 58369.40$ MJD (corresponding to Cycle 1), such that $\phi = 0.5$ corresponds to the peak of the activity of the source (see Pleunis et al. 2021, for further details).

The obtained phases for B1, B2, and B3 are reported in Table 2. From Fig. 4 we see that the three burst are consistently located within the predicted activity window of 5.2 days from CHIME/FRB, since our observational bandwidth overlaps with theirs (see again Pleunis et al. 2021, fig. 9). We do not report any detection from outside its window of activity (Fig. 4), consistently with the observed chromatic activity, as burst were detected at $\phi \sim 0.7$ at lower frequencies (Pastor-Marazuela et al. 2021; Pleunis et al. 2021).

4.3 Rate estimation and comparison with CHIME/FRB

We estimate the number of expected bursts at our facility for the monitored sources, making a comparison with the detection rates reported by CHIME/FRB, due to the partially overlapping

Downloaded from https://academic.oup.com/mnras/article/513/2/1858/6567872 by CNR user on 26 May 2022

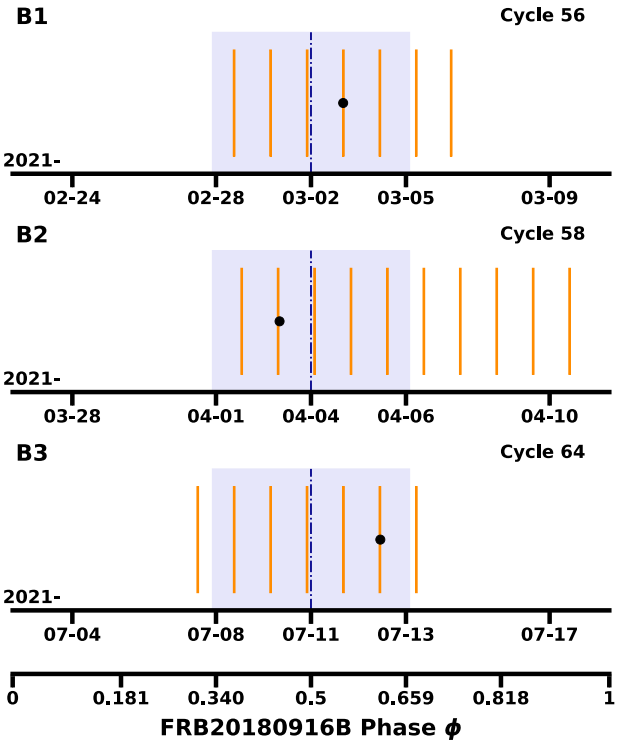


Figure 4. Bursts B1, B2, and B3 as a function of the periodicity phase ϕ. Orange bars show the NC observations during the source activity cycles (lavender rectangle). Cycle 1 corresponds to the first burst detection (CHIME/FRB Collaboration et al.2019a), with a starting epoch $\phi_0 = 58369.40$ MJD and $\phi = 0.5$ to be the centre of the activity window. Our detections (black circles) happened during Cycles 56, 58, and 64 respectively.

observational bandwidths. Let us assume that the differential number of bursts dN, for a facility x which operates at the central frequency ν_c^x, with fluence (or equivalently flux density for a 1 ms burst), within the interval (F, $F + \mathrm{d}F$) follows a power law of the kind:

$$\frac{\mathrm{d}N^x}{\mathrm{d}F} = K \left(\frac{\nu_c^x}{\nu_{\rm ref}}\right)^{-\beta} \left(\frac{F}{F_{\rm ref}}\right)^{-\alpha}, \tag{4}$$

where $F_{\rm ref}$, $\nu_{\rm ref}$ are, respectively, a reference fluence and a reference frequency, K corresponds to $\mathrm{d}N^x/\mathrm{d}F$ at $\nu = \nu_{\rm ref}$ and $F = F_{\rm ref}$, $\beta = 1.6 \pm 0.3$ (Macquart et al. 2019) is the spectral index, and lastly α is the slope of the differential fluence distribution (see The CHIME/FRB Collaboration et al. 2021, Section 6.2).[2] The value of α appears to be different for each source, with a value for instance of $\alpha = 2.3 \pm 0.4$ for FRB20180916B (CHIME/FRB Collaboration et al. 2020), although the possibility of a universal parameter for at least the class of repeaters is still open (see e.g. Marthi et al. 2022, for a discussion). Assuming that an FRB source is observed for an average observing time $\delta t_{\rm obs}^x$, we can evaluate the differential burst rate $\mathrm{d}R^x/\mathrm{d}F$ from equation (4) as

$$\frac{\mathrm{d}R^x}{\mathrm{d}F} = \frac{d^2N^x}{\mathrm{d}F\,\mathrm{d}t} = \frac{K}{\delta t_{\rm obs}^x} \left(\frac{\nu_c^x}{\nu_{\rm ref}}\right)^{-\beta} \left(\frac{F}{F_{\rm ref}}\right)^{-\alpha}. \tag{5}$$

[2]We consider a different convention for the slope α. Our α refers to the differential fluence distribution, whereas for the cited reference to the cumulative. The values of α reported in the reference, to be in accord with our convection, should be read as $-\alpha + 1$.

Henceforth, the expected detection rate of bursts with fluence exceeding a given threshold F_l^x is

$$R^x(F > F_l^x) = R^x = \frac{K}{\delta t_{\rm obs}^x} \left(\frac{\nu_c^x}{\nu_{\rm ref}}\right)^{-\beta} \int_{F_l^x}^{+\infty} \left(\frac{F}{F_{\rm ref}}\right)^{-\alpha} dF. \tag{6}$$

Taking $\alpha > 1$, we can ensure the convergence of the integral in equation (6) and we obtain the following expression:

$$R^x = \frac{K}{\delta t_{\rm obs}^x} \frac{1}{(\alpha - 1)} \left(\frac{\nu_c^x}{\nu_{\rm ref}}\right)^{-\beta} \left(\frac{F_l^x}{F_{\rm ref}}\right)^{-\alpha+1}. \tag{7}$$

Considering now equation (7) for both the NC and CHIME/FRB (CF) and calculating the ratios between the two equations, we can evaluate the rate of bursts expected at the NC with respect to the rate of bursts expected by CHIME/FRB as

$$R^{\rm NC} = R^{\rm CF} \left(\frac{\delta t_{\rm obs}^{\rm NC}}{\delta t_{\rm obs}^{\rm CF}}\right)^{-1} \left(\frac{\nu_c^{\rm NC}}{\nu_c^{\rm CF}}\right)^{-\beta} \left(\frac{F_l^{\rm NC}}{F_l^{\rm CF}}\right)^{-\alpha+1}. \tag{8}$$

Lastly, the average number of bursts $N^{\rm NC}$ that we expect at the NC, with fluence greater than $F_l{}^{\rm NC}$, throughout a campaign of total duration ΔT_c will be

$$N^{\rm NC} = R^{\rm NC}\, \Delta T_c. \tag{9}$$

4.3.1 *Instrument fluence detection threshold*

In order to evaluate the number of bursts throughout the campaign we need to estimate the minimum fluence detectable, given a certain threshold, we can achieve with the NC. In general, this fluence will depend on the physics which impact the arrived signal (e.g. the scattering) and also on the instrumental performances (e.g. the sampling time). From the radiometer equation we can compute the minimum flux density S_l', considering a minimum S/N of 10, we are able to detect with the NC (Burke-Spolaor et al. 2011):

$$S_l = S_l' \frac{\Delta t_m}{\Delta t}, \tag{10}$$

$$S_l' = 10 \times \frac{\mathrm{SEFD}^*}{A\sqrt{N_p N_c \Delta\nu_{ch} \Delta t}}\, \zeta\,(\mathrm{TOA}), \tag{11}$$

where

$$\Delta t_m = \sqrt{\Delta t^2 + t_{\rm DM}^2 + \tau^2 + t_s^2} \tag{12}$$

consists in the measured width of the burst, which will be generally broadened by the scattering time τ, the sampling time t_s of the receiver and the intrachannel smearing:

$$t_{\rm DM} = 8.3 \times 10^{-3} \left(\frac{\mathrm{DM}}{\mathrm{pc\ cm^{-3}}}\right) \left(\frac{\Delta\nu_{\rm ch}}{\mathrm{MHz}}\right) \left(\frac{\nu_c}{\mathrm{GHz}}\right)^{-3} \mathrm{ms}. \tag{13}$$

The quantity S_l' in equation (11) corresponds so to the minimum flux density detectable in the case of negligible intrachannel smearing, scattering, and sampling time. Considering now a nominal width of a burst of $\Delta t = 1$ ms and assuming $\zeta = 1.5$ throughout the whole transit of the source,[3] substituting all the numbers in equation (10) we can express the minimum detectable fluence (at 10σ) $F_l^{\rm NC}$ of the instrument as

$$F_l^{\rm NC} = S_l\,(\Delta t = 1\ \mathrm{ms}) \times 1\mathrm{ms} \tag{14}$$

$$= \frac{690.12}{\mathrm{A}} \frac{\sqrt{1.02 + t_{\rm DM}^2 + \tau^2}\,\mathrm{ms}}{1\ \mathrm{ms}}\ \mathrm{Jy\ ms}. \tag{15}$$

[3]ζ can actually vary between one and two throughout our observations, following the primary beam variations in a transit observation.

Downloaded from https://academic.oup.com/mnras/article/513/2/1858/6567872 by CNR user on 26 May 2022

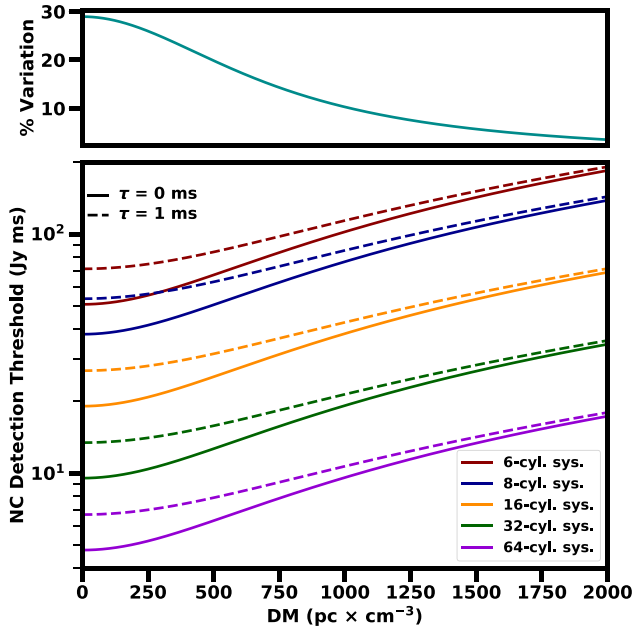


Figure 5. Northern cross fluence detection threshold curves. The bottom panel shows the NC fluence detection threshold as a function of the DM computed via equation (14) considering a scattering time $\tau = 0$ (solid lines) and 1 ms (dashed lines), for the previous 6-cylinder system (red), the current 8-cylinder system (blue) and the future 16-, 32-, 64-cylinder systems (orange, green, violet). The top panel represents the percentile variation between the threshold curve at $\tau = 1$ ms and the curve at $\tau = 0$.

Fig. 5 displays the fluence detection threshold of the NC, computed via equation (14), as a function of DM. In addition to the previously considered values of 24 and 32 for the six- and eight-cylinder systems, we consider $A = 64$, 128, 256 for the futures 16-, 32-, and 64-cylinder systems, respectively.

The scattering time is more uncertain to estimate, and we consider two cases: the case in which we neglect it and the case of a scattering time of 1 ms. From Fig. 5, we see the detection threshold increase as the DM increases, consistently with the fact the DM smearing dominates at higher DM. Regarding the scattering time, from the top panel of Fig. 5 we see that it is quite relevant at low DM, whereas for DMs higher than 1000 pc cm^{-3} the relative variation between the two defined regimes is below the 10 per cent.

We estimate the minimum fluence that can be detected from the monitored sources using equation (14) and assuming $\tau = 0$. In the case of FRB20180916B, we can detect bursts with fluences greater than 51 and 38 Jy ms for the six- and eight-cylinder system, respectively. FRB20181030A has been monitored only when the six-cylinder system was in place and we estimate a fluence detection threshold of 44 Jy ms. FRB20200120E and FRB20201124A were both monitored with the eight-cylinder system and we place for them, respectively, a fluence detection threshold of 33 and 42 Jy ms.

With current upgrades in progress, when the full North-South arm will be in use, we expect to find bursts, for instance from FRB20180916B, with 5 Jy ms fluence at S/N = 10.

4.3.2 *FRB20180916B*

Table 2 reports the flux densities and the fluences of the three bursts detected, computed from equation (3). We compute the expected number of bursts from FRB20180916B above our detection threshold by using equations (9) and (8). In order to do so, we make the following assumptions. The observing time of CHIME/FRB requires the knowledge of the time when the source was within the FWHM of their beam at 600 MHz: as observing time for CHIME/FRB, we assume 70 per cent of the computed transit time for the source,[4] yielding to 8.4 min. With the NC we observed the source for approximately 66 min every day of the campaign. We assume the burst rate to be 0.9 ± 0.5 h^{-1} above a fluence limit of 5.2 Jy ms within its activity window of 5.2 d (CHIME/FRB Collaboration et al. 2020). In Table 3, we report the expected number of bursts for $\sim$ 102 h (six-cylinders) and $\sim$ 70 h (eight-cylinders). We expect 1.4 ± 1.5 and 1.3 ± 1.2 bursts, respectively, and a total of 2.7 ± 1.9 bursts for the total monitoring of $\sim$180 h, consistent with our three detections. When the full North-South arm will be operational, we can expect $\sim$ 36 bursts from this source for a campaign of the same duration as the one performed.

Table 3. Results for the NC observational campaign. For each source, we report the observational system deployed (see Section 2) in the second column, the fluence detection threshold in the third column, and the total observing time in the fourth column. For FRB20180916B and FRB20201124A, we report in the fifth column the expected number of bursts $N^{\rm NC}$, whereas for the other two sources we report the 95 per cent confidence level lower limits of the slope of the differential fluence distribution α.

Source	System	$F_l^{\rm NC}$ (Jy ms)	ΔT_c (h)	$N^{\rm NC}$
FRB20180916B	Six	51	112.7	1.4 ± 1.5
	Eight	38	70.4	1.3 ± 1.2
			183.1	2.7 ± 1.9
FRB20201124A	Eight	44	68.14	1.0 ± 1.1
Source	System	$F_l^{\rm NC}$ (Jy ms)	ΔT_c (h)	α
FRB20181030A	Six	33	93.0	>2.1
FRB20200120E	Eight	42	109.2	>2.2

4.3.3 *FRB20181030A, FRB20200120E, and FRB20201124A*

No detections were obtained for FRB20181030A, FRB20200120E, and FRB20201124A after an observing campaign of 93, 109, and 68 h, respectively. We used our observations to constrain α, the slope of the fluence distribution for each source (see equation 4). Following Amiri et al. (2017) and Paper I, if we assume that the occurrence of a burst is a Poissonian process, we can compute the likelihood of detecting M bursts with expectation number $N(\alpha)$ [computing this with equations (8) and (9)] as

$$p\{M; N(\alpha)\} = \frac{N(\alpha)^M e^{-N(\alpha)}}{M!}. \quad (16)$$

The cumulative distribution function (CDF) of seeing X events lower than M, with $N(\alpha)$ expected, results then as the following expression:

$$P\{X < M | N(\alpha)\} = \sum_{k=0}^{M-1} p\{k; N(\alpha)\}. \quad (17)$$

Hence in the case of less than M = 1 events (non-detection case):

$$P\{X < M = 1 | N(\alpha)\} = e^{-N(\alpha)}. \quad (18)$$

In order to estimate $N(\alpha)$ we make some assumptions for the three sources. We separate the case of FRB20181030A and

[4]Source transit time can be computed thanks to the CHIME/FRB Online Calculator: https://www.chime-frb.ca/astronomytools

Downloaded from https://academic.oup.com/mnras/article/513/2/1858/6567872 by CNR user on 26 May 2022

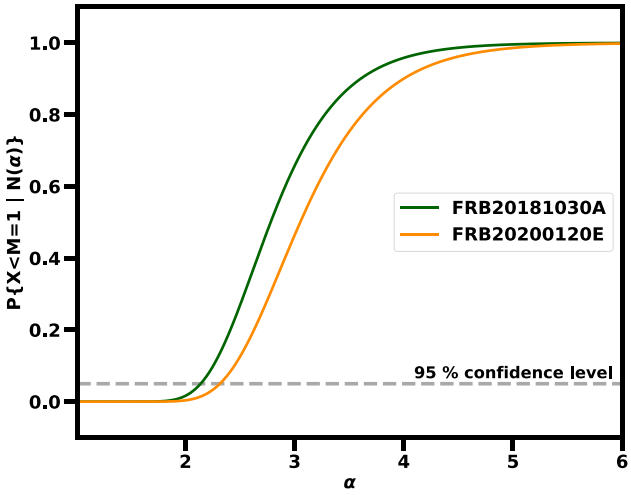


Figure 6. CDF of detecting zero events as a function of the slope of the differential fluence distribution α, for FRB20181030A (green line) and FRB20200120E (orange line). The horizontal dashed grey line demarcates the 5 per cent probability of not finding bursts from FRB20181030A (FRB20200120E) with α less than 2.1 (2.2), implying that α has to be greater than 2.1 (2.2) with a 95 per cent confidence level.

FRB20200120E from that of FRB20201124A for reasons that we report below.

Fig. 6 shows the CDF for the detection of zero events as a function of the slope α, for FRB20181030A and FRB20200120E, considering their respective total observing time (Table 3). In the cases of FRB20181030A and FRB20200120E, we assume a measured rate for CHIME/FRB equivalent to the predicted rate of the facility: $\sim$ 820 sky^{-1} d^{-1} above a threshold of 5 Jy ms at 600 MHz (The CHIME/FRB Collaboration et al. 2021). Under the same hypotheses as for FRB20180916B, we set 13 min as the average observing time at CHIME/FRB for FRB20181030A and 10 min for FRB20200120E. The average observing times at the NC for the two sources were 90 and 72 min, respectively.

Setting a confidence level of 95 per cent, from Fig. 6 we can rule out the values of α for which the probability computed by equation (18) is less than 0.05. The lower limits obtained for the values of α for both sources are reported in Table 3. These limits are consistent with the estimated values of α for a low-DM population as showed by The CHIME/FRB Collaboration et al. (2021). In their work, they searched for correlations between fluences and DMs among the current population of detected FRBs and found that the distributions of fluence versus α peak at two different values: $\alpha \sim 2$ for FRBs with DM between 100-500 pc cm^{-3} and $\alpha \sim 2.8$ for FRBs with DM $>$ 500 pc cm^{-3} (this retains the value of $\alpha = 2.5$, considering the whole sample of bursts, compatible with an Euclidean Universe).

In the case of FRB20201124A, Lanman et al. (2021) report a significant increase of the burst rate from the source in the period 2021 March–May with respect to the period between its discovery in 2020 November and 2021 March, implying a non-Poissonian distribution of the events.

Due to this non-Poissonianity, we only conservatively estimate the expected number of bursts above the estimated threshold for our facility for this source, in order to assess the compatibility with a non-detection. Following Lanman et al. (2021), we consider 4 min as the average observing time and a value of $\alpha = 4.5 \pm 2.2$ for CHIME/FRB. For CHIME/FRB, we assume a rate of 5.4 h^{-1} (see fig. 3 of the aforementioned paper) above a fluence limit of 17 Jy ms. We observed this source with NC for 120 min on average. The expected number of bursts from FRB20201124A for the NC was calculated as 1.0 ± 1.1, consistent with a non-detection.

5 CONCLUSIONS

This work presents the first FRB detections from the Medicina Northern Cross radio telescope, whose north–south arm is currently equipped to carry out FRB observations at 408 MHz with an observational bandwidth of 16 MHz. We performed a nineteen months observational campaign in which we targeted FRB20180916B, FRB20181030A, FRB20200120E, and FRB20201124A.

We describe the facility upgrade from the six-cylinder system to the eight-cylinder system. Before the upgrade we report the detection of a single burst from FRB20180916B above a 10σ fluence threshold of 51 Jy ms (which also accounts for the intra-channel smearing for our current frequency resolution of 14.468 kHz). After the upgrade we report the detection of two bursts from the same source above a fluence threshold of 38 Jy ms. All bursts were found within the 5.2 d activity window of the source, confirming the source periodicity. Assuming the CHIME/FRB source rate, we expected to detect 2.7 ± 1.9 bursts in our campaign, above the aforementioned fluence detection thresholds, consistent with our results.

We report no detections for the other three sources. In the cases of FRB20181030A and FRB20200120E, we constrain the slope of the differential fluence distribution α to be $\alpha > 2.1$ and $\alpha > 2.2$ at the 95 per cent confidence level, respectively. In the case of FRB20201124A we estimate 1.0 ± 1.1 bursts to be observed above a fluence detection threshold of 42 Jy ms, consistent with our non-detection.

SOFTWARE PACKAGES

Python Packages

BURSTFIT [5] (Aggarwal et al. 2021); MATPLOTLIB (Hunter 2007); NUMPY (Harris et al. 2020); SCIPY (Virtanen et al. 2020); YOUR[6](Aggarwal et al. 2020).

FRB/Pulsar softwares

DSPSR [7] (van Straten & Bailes 2011); FETCH[8] (Agarwal et al. 2020); HEIMDALL[9] (Barsdell et al. 2012); PRESTO[10] (Ransom et al. 2002); SIGPROC[11](Lorimer 2011); SPANDAK[12] (Gajjar et al. 2018).

ACKNOWLEDGEMENTS

The authors thanks the anonymous referee for the useful comments which significantly improved the quality of this work. The Northern Cross radio telescope is a facility of the University of Bologna operated under agreement by the Institute of Radio Astronomy of Bologna (Istituto Nazionale di Astrofisica, INAF). MT gratefully

[5] https://github.com/thepetabyteproject/burstfit
[6]https://github.com/thepetabyteproject/your
[7] http://dspsr.sourceforge.net/
[8]https://github.com/devanshkv/fetch
[9]https://sourceforge.net/projects/heimdall-astro/
[10]https://github.com/scottransom/PRESTO
[11]http://sigproc.sourceforge.net/
[12]https://github.com/gajjarv/PulsarSearch

Downloaded from https://academic.oup.com/mnras/article/513/2/1858/6567872 by CNR user on 26 May 2022

acknowledges INAF for the financial support for his PhD programme. NL acknowledges financial support from the European Research Council (ERC) under the European Union's Horizon 2020 research and innovation programme Hot-Milk (grant agreement No. [865637]).

DATA AVAILABILITY

The data presented in this paper and the software used can be shared upon reasonable request to the corresponding author.

REFERENCES

Agarwal D., Aggarwal K., Burke-Spolaor S., Lorimer D. R., Garver-Daniels N., 2020, MNRAS, 497, 1661
Aggarwal K. et al., 2020, J. Open Source Softw., 5, 2750
Aggarwal K., Agarwal D., Lewis E. F., Anna-Thomas R., Cardinal Tremblay J., Burke-Spolaor S., McLaughlin M. A., Lorimer D. R., 2021, ApJ, 922, 115
Amiri M. et al., 2017, ApJ, 844, 161
Barsdell B. R., Bailes M., Barnes D. G., Fluke C. J., 2012, MNRAS, 422, 379
Beloborodov A. M., 2017, ApJ, 843, L26
Bhardwaj M. et al., 2021a, ApJ, 910, L18
Bhardwaj M. et al., 2021b, ApJ, 919, L24
Burke-Spolaor S. et al., 2011, MNRAS, 416, 2465
Casentini C. et al., 2020, ApJ, 890, L32
Chatterjee S. et al., 2017, Nature, 541, 58
Chawla P. et al., 2020, ApJ, 896, L41
CHIME/FRB Collaboration et al., 2018, ApJ, 863, 48
CHIME/FRB Collaboration et al., 2019a, ApJL, 885, L24
CHIME/FRB Collaboration et al., 2019b, Nature, 566, 235
CHIME/FRB Collaboration et al., 2020, Nature, 582, 351
CHIME/FRB Collaboration et al., 2021, ApJS, 257, 59
CHIME/FRB Collaboration, 2021, Astron. Tel., 14497, 1
Comoretto G. et al., 2017, JAI, 06, 1641015
Cordes J. M., Chatterjee S., 2019, ARA&A, 57, 417
Cordes J. M., Lazio T. J. W., 2002, preprint (arXiv.astro-ph/0207156)
Cruces M. et al., 2021, MNRAS, 500, 448
Day C. K., Bhandari S., Deller A. T., Shannon R. M., Moss V. A., 2021, Astron. Tel., 14515, 1
Fong W.-f. et al., 2021, ApJ, 919, L23
Freedman W. L. et al., 1994, ApJ, 427, 628
Gajjar V. et al., 2018, ApJ, 863, 2
Ghisellini G., Locatelli N., 2018, A&A, 613, A61
Hankins T. H., Kern J. S., Weatherall J. C., Eilek J. A., 2003, Nature, 422, 141
Harris C. R. et al., 2020, Nature, 585, 357
Hessels J. W. T. et al., 2019, ApJ, 876, L23
Hunter J. D., 2007, Comput Sci Eng., 9, 90
Josephy A. et al., 2019, ApJ, 882, L18
Kirsten F. et al., 2021, Nature, 602, 585
Kumar P., Lu W., Bhattacharya M., 2017, MNRAS, 468, 2726
Kumar P., Shannon R. M., Moss V., Qiu H., Bhandari S., 2021, Astron. Tel., 14502, 1
Lanman A. E. et al., 2021, ApJ, 927, 59
Law C., Tendulkar S., Clarke T., Aggarwal K., Bethapudy S., 2021, Astron. Tel., 14526, 1
Locatelli N. T. et al., 2020, MNRAS, 494, 1229 (Paper I)
Lorimer D. R., 2011, Astrophysics Source Code Library, record(ascl:1107.016
Lorimer D., Kramer M., 2005, Handbook of Pulsar Astronomy Cambridge Observing Handbooks for Research Astronomers. Cambridge Univ. Press, Cambridge
Lu W., Kumar P., Zhang B., 2020, MNRAS, 898, 1397
Lyubarsky Y., 2014, MNRAS, 442, L9
Lyutikov M., Popov S., 2020, preprint (arXiv:2005.05093)
Macquart J. P., Shannon R. M., Bannister K. W., James C. W., Ekers R. D., Bunton J. D., 2019, ApJ, 872, L19
Majid W. A., et al. 2021, ApJL, 919, L6
Marcote B. et al., 2017, ApJ, 834, L8
Marcote B. et al., 2020, Nature, 577, 190
Marcote B. et al., 2021, Astron. Tel., 14603, 1
Marthi V. R. et al., 2022, MNRAS, 509, 2209
McKinnon M. M., 2014, PASP, 126, 476
Metzger B. D., Margalit B., Sironi L., 2019, MNRAS, 485, 4091
Michilli D. et al., 2018, Nature, 553, 182
Nicastro L., Guidorzi C., Palazzi E., Zampieri L., Turatto M., Gardini A., 2021, Universe, 7, 76
Nimmo K. et al., 2021a, NatAs, 6, 393
Nimmo K. et al., 2021b, ApJL, 927, L3
Pastor-Marazuela I. et al., 2021, Nature, 596, 505
Pearlman A. B., Majid W. A., Prince T. A., Nimmo K., Hessels J. W. T., Naudet C. J., Kocz J., 2020, ApJ, 905, L27
Perley R. A., Butler B. J., 2017, ApJS, 230, 7
Petroff E., Hessels J. W. T., Lorimer D. R., 2019, A&A Rev., 27, 4
Petroff E., Hessels J. W. T., Lorimer D. R., 2022, A&A Rev., 30, 2
Pilia M. et al., 2020, ApJ, 896, L40
Piro L. et al., 2021, A&A, 656, L15
Pleunis Z. et al., 2021, ApJ, 911, L3
Rajwade K. M. et al., 2020, MNRAS, 495, 3551
Ransom S. M., Eikenberry S. S., Middleditch J., 2002, ApJ, 124, 1788
Spitler L. G. et al., 2014, ApJ, 790, 101
Spitler L. G. et al., 2016, Nature, 531, 202
Tavani M. et al., 2020, ApJL, 893, L42
Tavani M. et al., 2021, NatAs, 5, 401
Tendulkar S. P. et al., 2017, ApJ, 834, L7
Tendulkar S. P. et al., 2021, ApJ, 908, L12
van Straten W., Bailes M., 2011, PASA, 28, 1
Verrecchia F. et al., 2021, ApJ, 915, 102
Virtanen P. et al., 2020, Nature Methods, 17, 261
Wharton R. et al., 2021, Astron. Tel., 14538, 1
Xu H. et al., 2021, Astron. Tel., 14518, 1
Zhang B., 2020, Nature, 587, 45

This paper has been typeset from a TEX/LATEX file prepared by the author.

Downloaded from https://academic.oup.com/mnras/article/513/2/1858/6567872 by CNR user on 26 May 2022